Highly Branched VS$_4$ Nanodendrites with 1D Atomic-Chain Structure as a Promising Cathode Material for Long-Cycling Magnesium Batteries

Yanrong Wang, Ziteng Liu, Caixing Wang, Xu Yi, Renpeng Chen, Lianbo Ma, Yi Hu, Guoyin Zhu, Tao Chen, Zuoxiu Tie, Jing Ma,* Jie Liu, and Zhong Jin*

Rechargeable magnesium batteries have attracted increasing attention due to the high theoretical volumetric capacities, dendrite formation-free characteristic and low cost of Mg metal anodes. However, the development of magnesium batteries is seriously hindered by the lack of capable cathode materials with long cycling life and fast solid-state diffusion kinetics for highly-polarized divalent Mg^{2+} ions. Herein, vanadium tetrasulfide (VS$_4$) with special one-dimensional atomic-chain structure is reported to be able to serve as a favorable cathode material for high-performance magnesium batteries. Through a surfactant-assisted solution-phase process, sea-urchin-like VS$_4$ nanodendrites are controllably prepared. Benefiting from the chain-like crystalline structure of VS$_4$, the S$_2^{2-}$ dimers in the VS$_4$ nanodendrites provide abundant sites for Mg^{2+} insertion. Moreover, the VS$_4$ atomic-chains bonded by weak van der Waals forces are beneficial to the diffusion kinetics of Mg^{2+} ions inside the open channels of VS$_4$. Through a series of systematic ex situ characterizations and density functional theory calculations, the magnesiation/demagnesiation mechanism of VS$_4$ are elucidated. The VS$_4$ nanodendrites present remarkable performance for Mg^{2+} storage among existing cathode materials, exhibiting a remarkable initial discharge capacity of 251 mAh g^{-1} at 100 mA g^{-1} and an impressive long-term cyclability at large current density of 500 mA g^{-1} (74 mAh g^{-1} after 800 cycles).

Rechargeable magnesium batteries have been considered as one of the most compelling candidates for large-scale sustainable electrochemical energy storage. Mg metal possesses several advantages, such as ultrahigh theoretical volumetric energy density (3833 mAh cm^{-3}), rich natural abundance,

and dendrite-free deposition during charging.[1–6] However, the strong electrostatic interactions between highly polarized divalent Mg^{2+} ions and host lattices of cathode material usually induce slow solid-state insertion/diffusion kinetics of Mg^{2+} ions within the crystal lattices.[7–10] In addition, the compatibility of existing electrode materials with only a handful of optional electrolytes is not satisfying, which also hinders the development of Mg batteries.[11–16] As a result, the search for cathode materials capable to reversibly intercalate Mg^{2+} with high capacity, long cycling life, and fast kinetics is quite challenging. Till now, one of the top-performing cathode material is Chevrel phase Mo$_6$S$_8$ reported by Aurbach et al.[1] Benefited from the moderate polarity of the anionic framework and the large size of the ion channels in Chevrel phase Mo$_6$S$_8$, the electrostatic interactions between Chevrel phase Mo$_6$S$_8$ and Mg^{2+} ions are relatively weak, thus favorable to the insertion of Mg^{2+} ions.[1] Up to now, only a few cathode materials with reasonable discharge capacity and cycling endurance for Mg batteries have been developed.[17–22] Among them, transition metal oxides (V$_2$O$_5$, MnO$_2$, Mn$_3$O$_4$) usually exhibit very sluggish kinetics and poor cycling stability.[23–26] Layered transition metal chalcogenides (TMCs, such as MoS$_2$,[17,27] WSe$_2$,[28] and TiS$_2$[29–31]) have been regarded as potential cathode materials for Mg batteries, because the "soft" anionic lattices (S or Se) contribute to a weaker Coulombic attraction with guest Mg^{2+} ions, which can enhance the mobility of Mg^{2+}, as well as the desolvation of Mg^{2+} at the electrolyte/electrode interface.[32,33] However, the TMCs usually suffer from narrow interlayer spacings that may hinder the diffusion of Mg^{2+} ions, therefore to expand the interlayer spacings of TMCs is essential for improving the magnetization/demagnetization kinetics.

Herein, we first propose that VS$_4$ with special atomic-chain structure can serve as a novel and promising cathode material with high capacity and long cycling life for Mg batteries. In the history, VS$_4$ was first discovered from patronite mineral in 1906,[34] and its crystalline structure was elucidated in 1964.[35] It has been revealed that VS$_4$ is a "linear-chain" compound

Y. R. Wang, Z. T. Liu, C. X. Wang, X. Yi, R. P. Chen, L. B. Ma, Y. Hu, G. Y. Zhu, T. Chen, Z. X. Tie, Prof. J. Ma, Prof. J. Liu, Prof. Z. Jin
Key Laboratory of Mesoscopic Chemistry of MOE
School of Chemistry and Chemical Engineering
Nanjing University
Nanjing 210023, China
E-mail: majing@nju.edu.cn; zhongjin@nju.edu.cn
Prof. J. Liu
Department of Chemistry
Duke University
Durham, NC 27708, USA

The ORCID identification number(s) for the author(s) of this article can be found under https://doi.org/10.1002/adma.201802563.
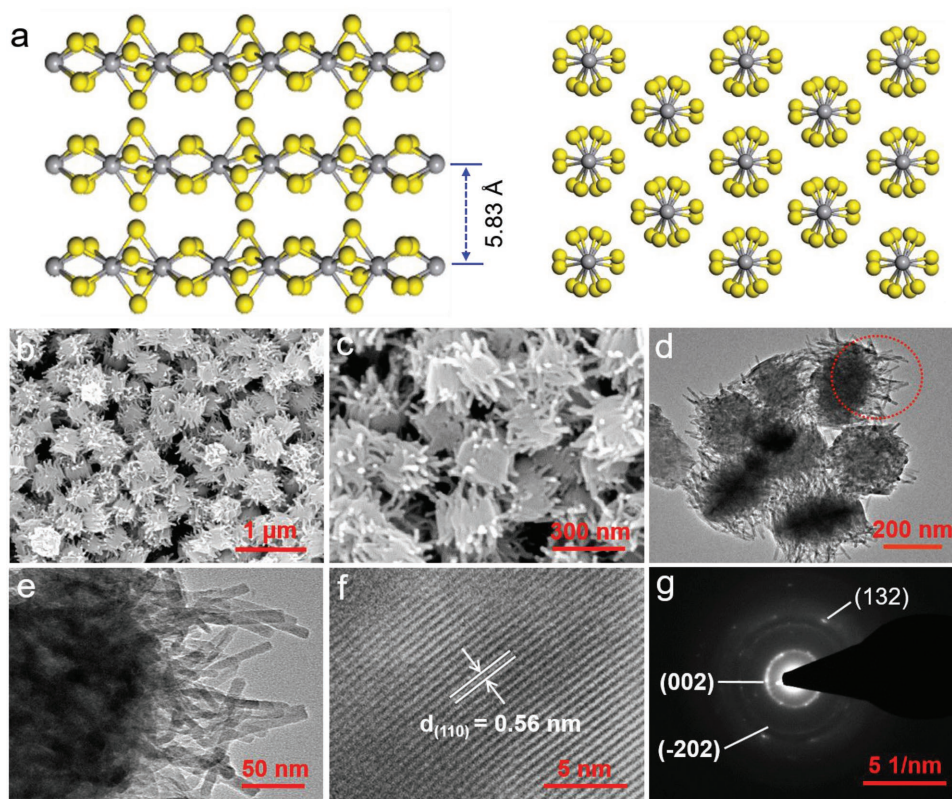
Figure 1. Schematic geometries of VS$_4$ and morphology characterizations of VS$_4$ nanodendrites. a) Lateral-view (left) and vertical-view (right) of the "linear-chain" crystalline structure of VS$_4$, showing an interval of 5.83 Å between the atomic chains. b–g) Morphology characterizations of VS$_4$ nanodendrites: b,c) SEM images, d,e) TEM images, f) HRTEM image, g) SAED pattern of VS$_4$ nanodendrites.

composed of V^{4+} ions coordinated to sulfur dimers (S$_2^{2-}$) extending along the c axis,[36] as shown in **Figure 1**a. The individual atomic chains of VS$_4$ are only bonded by weak van der Waals forces, which provide a loosely stacking structure. Previous researches showed that VS$_4$ appeared to display a Peierls distortion and exhibits a narrow bandgap of ≈1.0 eV and relatively high electronic conductivity.[37,38] The interval between the atomic chains of VS$_4$ is 5.83 Å, which is much larger than the effective ionic diameter of Mg^{2+} (1.44 Å). The open channels between the atomic chains of VS$_4$ offer abundant active sites for Mg^{2+} diffusion and storage. Moreover, the interactions between neighboring atomic chains are quite weak, thus can favorably facilitate the ion-transfer kinetics of Mg^{2+}. However, the systematic study of VS$_4$ was rare in the literature by the fact that the synthesis of pure VS$_4$ was difficult.[39] To date, only very few efforts have been made to the Li$^+$ and Na$^+$ storage in VS$_4$.[38,40–42] In 2015, Grey and co-workers have revisited the reversible lithiation of VS$_4$ to determine its multiple redox modes by employing a series of structural characterization tools.[36]

To the best of our knowledge, so far, the reversible electrochemical storage of Mg^{2+} ions in VS$_4$ has not been reported yet. Herein, we develop a convenient solution-phase process to prepare highly branched VS$_4$ nanodendrites assembled by numerous 1D VS$_4$ nanorods. The VS$_4$ nanodendrites exhibit ultrahigh reversible capacity, exceptional rate performance, and excellent cycling stability superior to those of other cathode materials for Mg batteries. The reversible

magnetization/demagnetization mechanism in VS$_4$ was scrutinized by ex situ X-ray photoelectron spectroscopy (XPS), ex situ X-ray diffraction (XRD), ex situ Raman spectroscopy and density functional theory (DFT) calculations. The Mg^{2+} transport/diffusion properties and the special internal redox behaviors in VS$_4$ were also elucidated in detail.

For the synthesis of VS$_4$ nanodendrites, a solvothermal reaction of NH$_4$VO$_3$ and thioacetamide (TAA) was performed in a mixed ethylene glycol (EG)/water solution at 160 °C for 12 h in the presence of block copolymer F127 as surfactant (see Experimental Section). Resulted from the sulfuration effect of TAA and the morphology control by F127 surfactant, sea urchin-like VS$_4$ nanodendrites with multibranching structure were obtained. Scanning electron microscopy (SEM) and transmission electron microscopy (TEM) characterizations revealed the morphology of VS$_4$ nanodendrites with a uniform size of ≈300 nm assembled by many agminated nanorods with an average diameter of ≈10 nm (Figure 1b–e). The high-resolution TEM (HRTEM) image in Figure 1f shows a lattice plane spacing of 0.56 nm in VS$_4$ nanodendrites, corresponding the (110) planes of monoclinic phase VS$_4$. The selected area electron diffraction (SAED) pattern (Figure 1g) consisting of diffused diffraction rings can be congruously indexed to the monoclinic phase of VS$_4$ (JCPDS card No. 72-1294, space group $I2/c$, $a = 6.8$, $b = 10.4$, $c = 12.1$).

X-ray powder diffraction (XRD) patterns confirmed the good crystallinity and high purity of as-obtained VS$_4$ nanodendrites
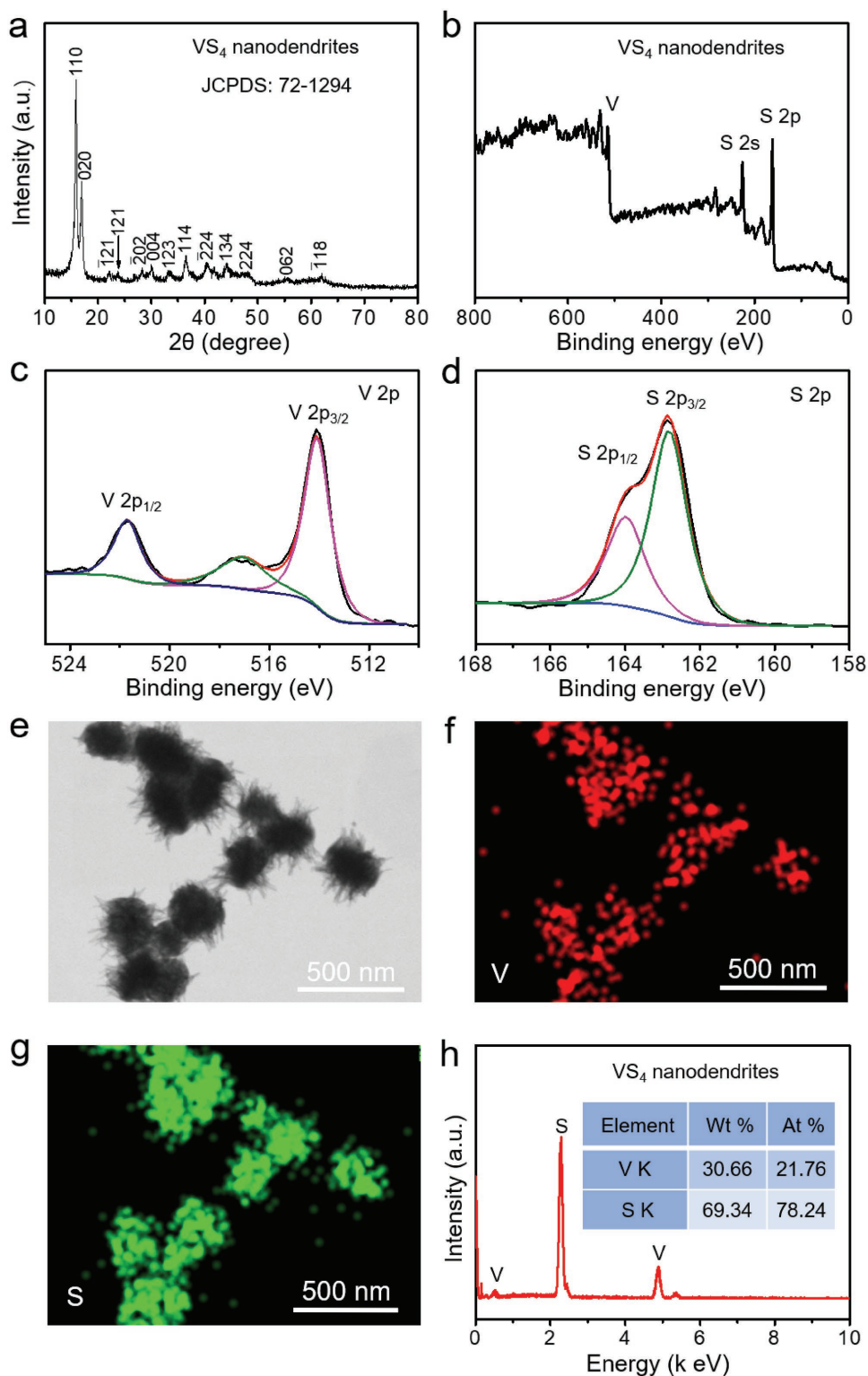
**ADVANCED
SCIENCE NEWS**
www.advancedsciencenews.com

**ADVANCED
MATERIALS**
www.advmat.de

Figure 2. Structural and composition characterizations of VS_4 nanodendrites. a) XRD pattern, b) survey XPS spectrum, high-resolution XPS spectra at c) V 2p and d) S 2p core level regions, e) BF-STEM image, f,g) corresponding areal mappings of V (f) and S (g) elements, and h) EDX analysis of VS_4 nanodendrites.

(**Figure 2**a), and all the reflection peaks were well assigned to monoclinic phase VS_4. XPS analysis revealed the coexistence and the valence states of V and S elements (Figure 2b–d). The

energy bands at 514.1 and 521.7 eV are attributed to V $2p_{3/2}$ and V $2p_{1/2}$ bands (Figure 2c), which are the characteristic features of V^{4+} rather than V^{5+} (V 2p peak of V^{5+} are normally located

at ≈517.2 and 524.5 eV),[18,43–45] indicating the domination of V^{4+} in VS_4 nanodendrites. The high-resolution XPS scanning at S 2p region demonstrated the existence of S_2^{2-} dimers (Figure 2d), and the peaks at 162.9 and 164.0 eV were ascribed to S $2p_{3/2}$ and S $2p_{1/2}$ bands, respectively. Differently, the peaks of S $2p_{3/2}$ and S $2p_{1/2}$ in vanadium disulfide (VS_2, containing S^{2-} instead of S_2^{2-}) appears at around 162.5 and 163.5 eV, respectively,[46,47] which are at lower energy levels than those of VS_4 (with S_2^{2-}) in this work. Bright-field scanning TEM (BF-STEM) and corresponding energy dispersive X-ray spectroscopy (EDX) elemental analysis (Figure 2e–h) clearly show the evenly distributed V and S atoms with an atomic ratio around 1:4, which is consistent to the analytical results of XPS.

Furthermore, a set of control experiments of VS_4 synthesis were carried out to investigate and adjust the formation process of the VS_4 nanodendrites. Figure S1 (Supporting Information) shows the SEM images of four different samples of VS_4 nanostructures prepared with distinct reaction times. In the early reaction period, small VS_4 nanoparticles were first obtained (Figure S1a, Supporting Information). As the reaction time went on, the product started to show the nanodendrite-like morphology (Figure S1b, Supporting Information), and the diameter and length of VS_4 nanorods composing nanodendrites

gradually increased as the reaction time was extended (Figure S1c,d, Supporting Information). To investigate the effect of F127 surfactant on the morphology of products, a control sample was prepared without adding F127 while keeping other conditions unchanged. Interestingly, only uniform VS_4 nanospheres with ≈500 nm in diameter were obtained (Figure S2a,b, Supporting Information). The HRTEM interplanar spacing and XRD pattern of VS_4 nanospheres (Figure S2c,d, Supporting Information) are also in accordance with monoclinic phase VS_4. Figure S3 (Supporting Information) shows the measured surface area of VS_4 nanodendrites and VS_4 nanospheres are 41.7 and 38.8 m^2 g^{-1}, respectively. Compared to VS_4 nanospheres, we expect that the high-branched VS_4 nanodendrites consisted of nanorods can better improve the electrical conductance between each other and facilitate the transport of electrons and Mg^{2+} ions during discharge/charge cycles (as experimentally confirmed below), thus conducive to the utilization ratio of active material and the rate capability.

The Mg^{2+} storage properties of VS_4 nanodendrites as cathode material for Mg batteries were systematically investigated. **Figure 3**a shows the typical CV curves of VS_4 nanodendrites at a scan rate of 0.2 mV s^{-1}. The voltage range was set between 0.2 and 2.2 V to prevent strong polarization and electrolyte
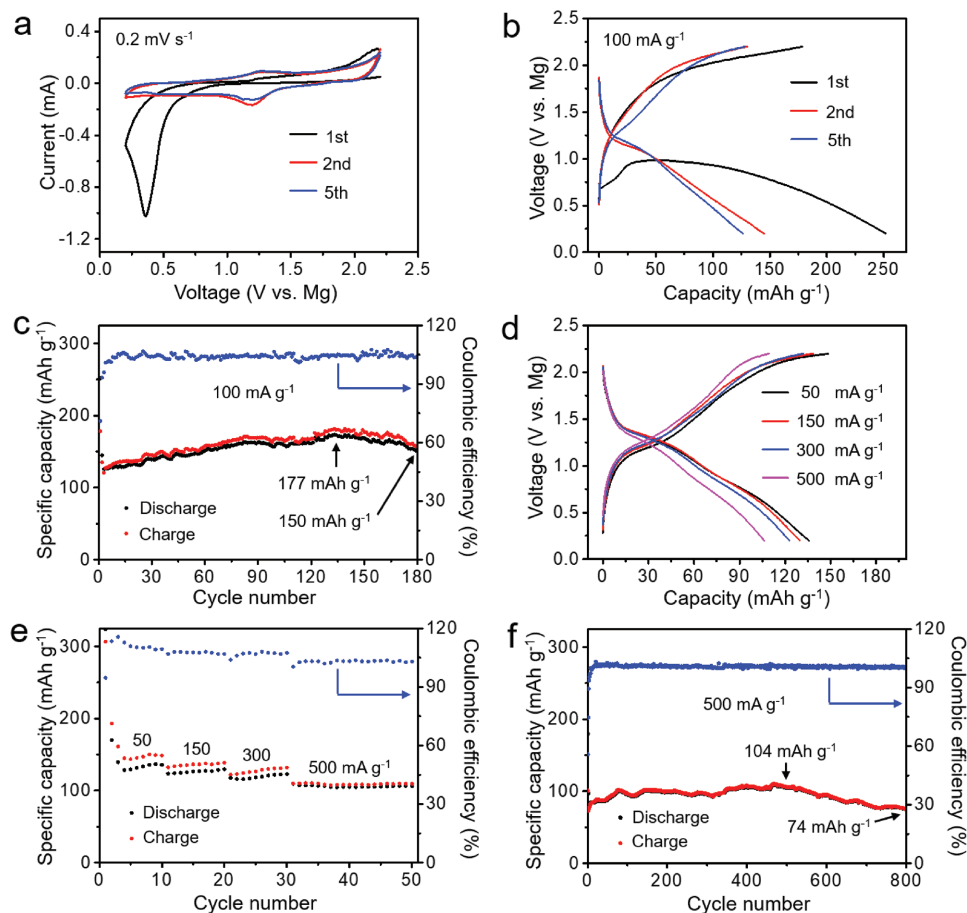

Figure 3. Electrochemical performances of Mg batteries with VS_4 nanodendrites as cathodes. a) CV curves measured in a voltage range between 0.2 and 2.2 V at a scanning rate of 0.2 mV s^{-1}. b) Discharge–charge curves and c) cycling performance at a current density of 100 mA g^{-1}. d) Discharge–charge curves and e) rate performance at the current densities ranged from 50 to 500 mA g^{-1}. f) Long-term cycling test at 500 mA g^{-1} for 800 cycles.

**ADVANCED
SCIENCE NEWS**

www.advancedsciencenews.com

**ADVANCED
MATERIALS**

www.advmat.de

decomposition.[20–22,27,31] The CV curve at the first cycle shows a strong reduction peak ≈0.35 V. Compared to the subsequent cycles, the relatively strong polarization in the first discharge process is probably caused by the presence of oxide layer on the surface of Mg anode.[48] During the second cycle, a reduction peak appears at ≈1.18 V and an oxidation peak appears at ≈1.25 V versus Mg^{2+}/Mg, resulting from the Mg^{2+} insertion into VS_4 and the Mg^{2+} extraction from VS_4, respectively. The characteristics of CV curves in the following cycles are similar to the second cycle. Figure 3b shows the discharge–charge curves of VS_4 nanodendrites at a current density of 100 mA g^{-1}. An initial discharge capacity of 251 mAh g^{-1} was obtained, corresponding to the formation of $Mg_{0.84}VS_4$ (1 C = 1 Mg^{2+}/VS_4). The following charge capacity is 179 mAh g^{-1}, corresponding to a Coulombic efficiency of ≈71.3%, which suggests that some Mg^{2+} ions are still trapped in the VS_4 lattices ($Mg_{0.24}VS_4$) after the first charge step. As estimated by EDX, the atomic contents at the end of the first discharge and charge steps were shown in Figure S4a,b (Supporting Information), respectively, which is in agreement with the measured capacities. The discharge and charge capacities were found to be 126 and 128 mAh g^{-1} in the fifth cycle, respectively, with a greatly improved Coulombic efficiency of about 101.6%, which could be ascribed to the electrode activation and the extraction of more Mg^{2+} ions.

Figure 3c presents the cycling performance of VS_4 nanodendrites at 100 mA g^{-1}. There is an activation process during the first few cycles, and the polarization decreases in the subsequent cycles. The reversible capacity progressively increases and ultimately reaches a maximum discharge capacity of 177 mAh g^{-1} after 133 cycles, and retains 150 mAh g^{-1} at the 180 cycles with Coulombic efficiency kept at ≈104.0%. Figure 3d,e shows the discharge–charge curves and rate capability of VS_4 nanodendrites cycling at different current densities ranged from 50 to 500 mA g^{-1}. The discharge capacities are 137, 130, 123, and 106 mAh g^{-1} at 50, 150, 300, and 500 mA g^{-1}, respectively, showing a retention ratio of 77% as the current rate increases from 50 to 500 mA g^{-1}. The long-term cycling stability of VS_4 nanodendrites at a high current density of 500 mA g^{-1} is shown in Figure 3f. The initial discharge and charge capacities are 179 and 100 mAh g^{-1}, respectively, with an initial Coulombic efficiency of 55.9%. The discharge and charge capacities at the fifth cycle are 79 and 82 mAh g^{-1}, respectively, with a Coulombic efficiency of 96.3%. The discharge and charge capabilities increase to 105 and 105.6 mAh g^{-1} after 500 cycles, respectively, with a Coulombic efficiency of 100.6% and remain at 75.2 and 75.3 mAh g^{-1} with the Coulombic efficiency of nearly 100% even after 800 cycles. From the above results, the Coulombic efficiency at relative high current density is improved to nearly 100% compared with lower current density, which could be ascribed to self-discharge phenomenon at lower current density.[10] Such an impressive cycling stability for Mg^{2+} storage should be attributed to the unique atomic-chain structure of VS_4 and the weak interactions between the VS_4 and Mg^{2+}. The linear open channels in VS_4 are favorable for the Mg^{2+} diffusion/migration and the S_2^{2-} dimers provide sufficient active sites that can store a huge amount of Mg^{2+} ions, thus leading to the high reversible capacity, rate performance, and cyclicity.

For comparison, we also investigated the Mg^{2+} storage properties of VS_4 nanospheres. As shown in Figure S5

(Supporting Information), the capacity and rate capability of VS_4 nanospheres is inferior to those of VS_4 nanodendrites. The electrochemical impedance spectroscopy (EIS) analyses of the VS_4 nanodendrites and nanospheres are shown in Figure S6a (Supporting Information). The semicircles in high frequency and sloping lines in low-frequency in the Nyquist plots are associated with the charge transfer kinetics at the electrode/electrolyte interface (R_{ct}) and the Mg^{2+} diffusion resistance within the electrodes, respectively. The VS_4 nanodendrites electrode shows lower resistance values than that of VS_4 nanospheres, confirming that the high-branched hierarchical structures of VS_4 nanodendrites are beneficial to the formation of conductive network for facilitating electron and Mg^{2+} diffusion transfer, thus conducive to the capacity and rate performance. The EIS analysis of VS_4 nanodendrites electrode after 20 cycles at 100 mA g^{-1} was also performed, as shown in Figure S6b (Supporting Information). The R_{ct} and Mg^{2+} diffusion resistance values of VS_4 nanodendrites were greatly decreased after 20 cycles due to the activation process in the previous cycles, which was also the reason of capacity increase after the initial cycle. Galvanostatic intermittent titration technique (GITT) was utilized to estimate the polarization of VS_4 nanodendrites cathode. Figure S7 (Supporting Information) shows the GITT curves of VS_4 nanodendrites cathode measured at 50, 100, and 150 mA g^{-1}, respectively. It is found that GITT curves measured at these large current densities display small potential gaps between the operating and equilibration states, indicating the small ohmic polarization that is conducive to the rate performance.[6,31]

To investigate the magnetization/demagnetization processes in VS_4 nanodendrites, ex situ XPS, ex situ XRD, and ex situ Raman spectroscopy were performed in various stages. **Figure 4**a–c shows a set of ex situ XPS spectra at V 2p, S 2p, and Mg 2p regions acquired from pristine, discharged and charged VS_4 nanodendrites cathodes, respectively. In Figure 4a, the high-resolution V 2p XPS spectrum of pristine cathode shows two peaks at 514.0 eV (V $2p_{3/2}$ band for V^{4+}) and 521.6 eV (V $2p_{1/2}$ band for V^{4+}), respectively, comparable to Figure 2c. After discharged to 0.2 V, the significantly increased intensities of energy bands at 516.9 eV (V $2p_{3/2}$ band for V^{5+}) and 524.4 eV (V $2p_{1/2}$ band for V^{5+}) indicate the partial oxidation of V^{4+} to V^{5+}. According to the XPS results, the atomic ratio of V^{4+}:V^{5+} after discharge was calculated to be 13:87 (Table S2, Supporting Information). When charged again to 2.2 V, the V 2p XPS spectrum still could be indexed into four peaks, but the atomic ratio of V^{4+}:V^{5+} increased to 23:77.

In Figure 4b, the high-resolution XPS spectrum of pristine VS_4 nanodendrites shows two peaks at 162.9 and 164.1 eV, which are comparable to those in Figure 2d, corresponding to the S $2p_{3/2}$ and S $2p_{1/2}$ bands of S_2^{2-}, respectively. After discharged to 0.2 V, the XPS curve at S 2p region shows two newly emerging deconvoluted peaks located at 162.6 eV (S $2p_{3/2}$ band for S^{2-}) and 163.8 eV (S $2p_{1/2}$ band for S^{2-}), respectively, confirming the partial reduction of S_2^{2-} to S^{2-} by the insertion of Mg^{2+}. The minimal peak ≈160.8 eV is originated from the interaction between Mg^{2+} and sulfur species. The atomic ratio of S_2^{2-} and S^{2-} species quantified by the XPS results (Table S2, Supporting Information) is ≈42:58. After charged to 2.2 V, the high-resolution spectrum of S 2p can be indexed into four main

**ADVANCED
SCIENCE NEWS**

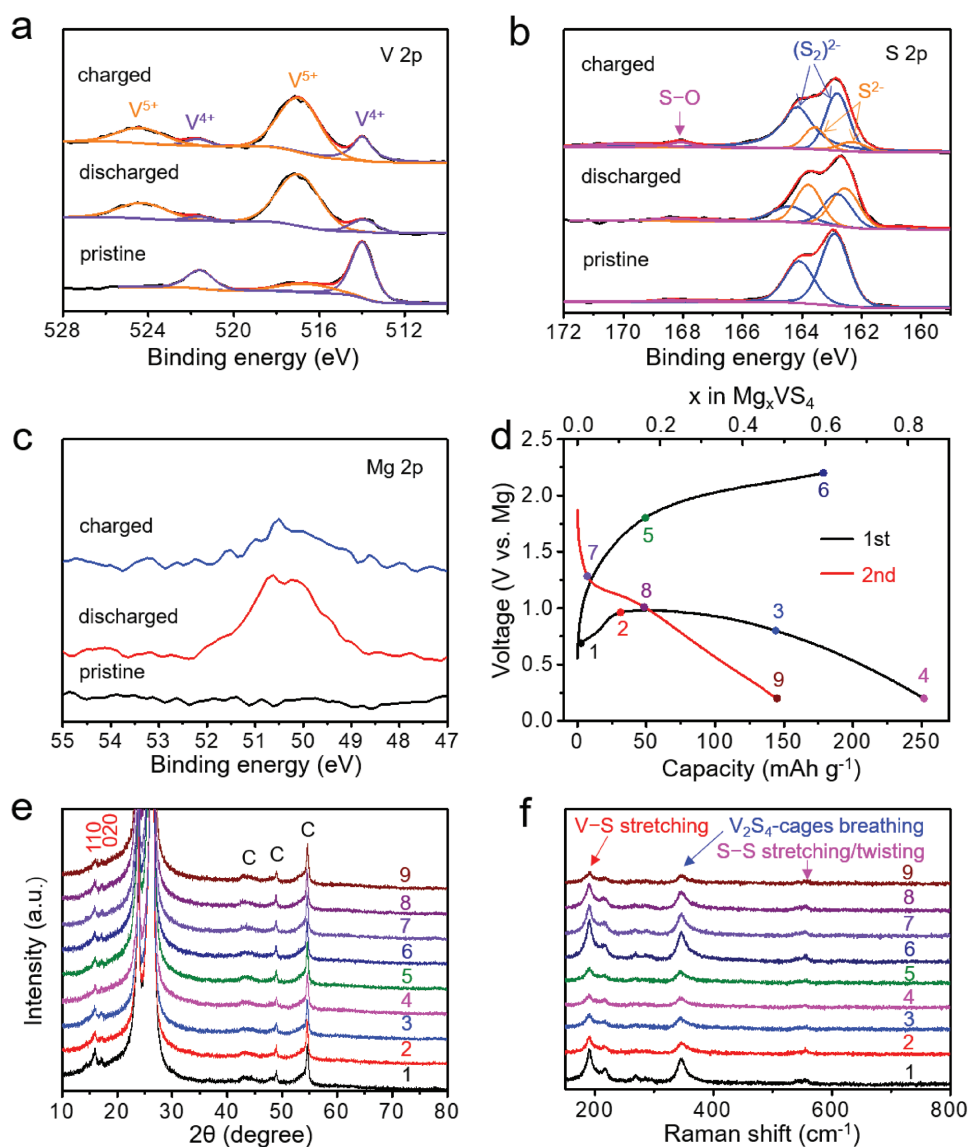www.advancedsciencenews.com

**ADVANCED
MATERIALS**

www.advmat.de

Figure 4. Investigation of the magnetization/demagnetization processes in VS$_4$ nanodendrites. a–c) Ex situ high-resolution XPS spectra at the V 2p (a), S 2p (b), and Mg 2p (c) regions of VS$_4$ nanodendrites cathode at the pristine state, after the first discharge step and after the first charge step, respectively. d) Electrochemical discharge–charge profiles of VS$_4$ nanodendrites cathode during the first and second cycles at a current density of 100 mA g^{-1}. The points labeled with 1 to 9 indicate the different discharge–charge states at which the XRD patterns in (e) and the Raman spectra in (f) were collected. e) Ex situ XRD patterns of VS$_4$ nanodendrites collected at various discharge–charge states. The peaks labeled by "C" are originated from carbon paper served as current collector. f) Ex situ Raman spectra of VS$_4$ nanodendrites collected at various discharge–charge states.

peaks. The peaks at 162.8 and 164.1 eV are assigned to S$_2^{2-}$, and the two peaks at 162.4 and 163.6 eV are attributed to S^{2-}, respectively. After charging, the ratio of S$_2^{2-}$ and S^{2-} species increased to about 81:19 (Table S2, Supporting Information). The tiny peaks located at around 167.3 and 168.6 eV for the discharged sample, and the peaks located at around 168.1 and 170.0 eV for the charged sample indicate the formation of S—O bonds, which is attributed to the degradation of THF solvent.[21] The valence state changes of V and S atoms are mainly owing to the charge transfer between Mg^{2+} ions and VS$_4$, which is confirmed by DFT calculations (detailed below).

In Figure 4c, the high-resolution XPS spectra at Mg 2p region of discharged and charged VS$_4$ nanodendrites cathodes

both show Mg 2p peaks located at ≈50.4 eV, which is between the values of metallic Mg (≈49.5 eV) and Mg^{2+} (≈50.8 eV),[49,50] indicating the inserted Mg ions can take negative charges (electrons) from VS$_4$, thus leading to the valence changes of V and S atoms. The intensity of Mg 2p band after the first discharge step is higher than that after the first charge step, confirming the reversible insertion/extraction of Mg^{2+} into/from VS$_4$, which is consistent with the EDX results (Figure S4, Supporting Information), and also indicating that there are some Mg^{2+} ions remained in the VS$_4$ lattices during the discharge/charge processes.

The HRTEM images of both the discharged and charged VS$_4$ nanodendrites show the same lattice spacing of 0.56 nm

**ADVANCED
SCIENCE NEWS**

www.advancedsciencenews.com

**ADVANCED
MATERIALS**

www.advmat.de

corresponding to the (110) planes (Figure S8, Supporting Information), which is identical to the pristine VS_4 nanodendrites, indicating that the insertion of Mg^{2+} ions have very slight influence to the lattice parameters of VS_4. The ex situ XRD patterns of the VS_4 nanodendrites electrode at different discharge–charge states (from state 1 to state 9 in Figure 4d) were also measured, as shown in Figure 4e. The original electrode (state 1) shows two main peaks at 15.8° and 17.0°, which are attributed to the (110) and (020) planes of monoclinic-phase VS_4, respectively. The positions of these two peaks remained unchanged during the discharge/charge processes; however, the intensities of these two peaks changed apparently (Figure 4e). As discharged to 0.2 V in the first discharge step (from state 1 to state 4), the (110) and (020) peak intensities gradually decreased, resulting from the insertion of Mg^{2+} ions between VS_4 atomic-chains. Subsequently, the peak intensities increased again during the following first charge step (from state 4 to state 6), on account of the partial extraction of Mg^{2+} ions. In the second discharge step (from state 7 to state 9), the peak intensities gradually decreased again, confirming the good reversibility.
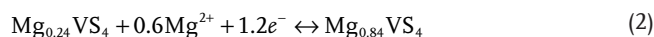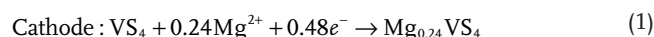
Figure 4f shows the ex situ Raman spectra of VS_4 at different discharge–charge states. The Raman spectrum of pristine VS_4 nanodendrites electrode (state 1) shows several characteristic peaks. The peaks located at 191 and 218 cm^{-1} correspond to the stretching modes of V−S bonds. The peak at 270 cm^{-1} is attributed to the bending mode of V−S bonds. The peak at 346 cm^{-1} is a breathing mode of the V_2S_4 cages. The other peaks located at 285, 543, and 557 cm^{-1} are attributed to S−S bond stretching/twisting.[42,51,52] During the discharge/charge processes, the positions of these peaks remained almost unchanged and there were no new peaks emerged, but obvious changes of peak intensities were observed (Figure 4f). During the first discharge step (from state 1 to state 4), the Raman peaks became weaker and broader, corresponding to the insertion of Mg^{2+} ions into VS_4, similar to the above XRD results. Then, the peak intensities gradually recovered again (from state 4 to state 6), owing to the partial extraction of Mg^{2+} ions. In the second discharge step (from state 6 to state 9), the Raman peaks become weaker and broader again. We also examined the morphology change, ex situ XPS, ex situ XRD, and ex situ Raman spectra of discharged and charged VS_4 nanodendrites cathode after 20 cycles (Figures S9 and S10, Supporting Information). The morphology of the VS_4 nanodendrites showed very little change after 20 cycles. The corresponding changes of atomic ratios ($V^{4+}:V^{5+}$ and $S_2^{2-}:S^{2-}$) after 20 cycles are shown in Table S2 (Supporting Information). These results display the change trends (valance states of V and S, contents of Mg^{2+} ions, intensities of XRD and Raman peaks, etc.) similar to the first discharge/charge cycle, indicating the good reversibility of Mg^{2+} insertion/extraction.

To further investigate the magnetization/demagnetization mechanism of VS_4, DFT calculations were also performed. Aiming to closely correlate with the experimental results of Mg contents (from 0 to 0.84), the supercell models of $Mg_{8x}V_8S_{32}$ (with $n = 8$, which is the number of VS_4 cell) were selected for representing Mg_xVS_4 ($x = 0$ to 0.875), as shown in Figures S11 and S12 (Supporting Information). The results of DFT simulation with PBE (Perdew–Burke–Ernzerhof) functional demonstrate that the introduction of Mg^{2+} ions into VS_4 has minor

influence on the average lattice parameters (when $x = 0.25$, $a/b/c \approx 7.2/10.9/12.1$ Å; when $x = 0.875$, $a/b/c \approx 7.0/10.9/12.3$ Å, as shown in Table S3 in the Supporting Information) in comparison with pristine VS_4 ($a/b/c = 6.8/10.4/12.1$ Å obtained from XRD analysis, consistent well with JCPDS card No. 72-1294). All combinations of possible insertion positions of Mg^{2+} ions and corresponding optimized structures of Mg_xVS_4 with different Mg^{2+} insertion content x (from 0 to 0.875) are given in Table S3 (Supporting Information). The changes in electronic structures of Mg_xVS_4 upon the discharging process are also presented by the DFT calculation results of relative formation energy (**Figure 5**a) and charge density distribution (Figure 5b). Figure 5a displays the possible geometries of Mg_xVS_4 corresponding to the lowest relative formation energies among various possible insertion positions of Mg^{2+} ions. The calculation results confirm that the discharging process with Mg^{2+} insertion into Mg_xVS_4 is energetically favorable when $0 \leq x \leq 0.875$. Specifically, from Table S3 (Supporting Information) and Figure 5a, the average relative formation energies tend to decrease when Mg content x increases from 0.125 to 0.625, indicating that the insertion of more Mg^{2+} ions is energetically more favorable. However, with further more Mg^{2+} ions intercalated into Mg_xVS_4 ($0.625 < x \leq 0.875$), the relative formation energy of Mg_xVS_4 gradually increases along with the increase of Mg^{2+} content, but still energetically favorable.

The addition of Mg^{2+} ions significantly affects the charge density distribution of the adjacent V and S atoms (Figure 5b). The DFT calculation results also show that the charge transfer between Mg^{2+} ions and VS_4 leads to an average charge transfer number of ≈1.0 per every intercalated Mg^{2+} ion (Figure S13, Supporting Information), which closely correlate with the valance state changes of V and S atoms in Mg_xVS_4 revealed by XPS results (Figure 4a,b). Some partially distorted structures of Mg_xVS_4 were also located by DFT calculations, as shown in Figure S14 (Supporting Information). Most of those site-disordered geometries are energetically unfavorable than those ordered ones given in Figure 5a. To our surprise, no matter with or without the site-distortion, the calculated lattice parameters of Mg_xVS_4 ($0 < x \leq 0.875$) keeps nearly constant with the maximum variation being less than 4.7% relative to the pristine VS_4. This rationalizes well the reversible insertion/extraction of Mg ions into/from VS_4, and also confirms that the structure of the Mg_xVS_4 has very little distortion upon Mg cycling.

According to the above detailed characterizations and DFT calculations, we conclude that the insertion of Mg^{2+} ions into VS_4 during the discharge steps forms Mg_xVS_4, resulting in the partial reduction of S_2^{2-} to S^{2-} and the partial oxidation of V^{4+} to V^{5+}. On the contrary, the extraction of Mg^{2+} ions from VS_4 during the charge steps makes the Mg^{2+} content decreasing from approximately $Mg_{0.84}VS_4$ to $Mg_{0.24}VS_4$, and the valence states of most V^{5+} and S^{2-} changes back to V^{4+} and S_2^{2-}. As illustrated in Figure 5c, the working mechanism of Mg–VS_4 batteries in the two electrodes can be approximately represented as below

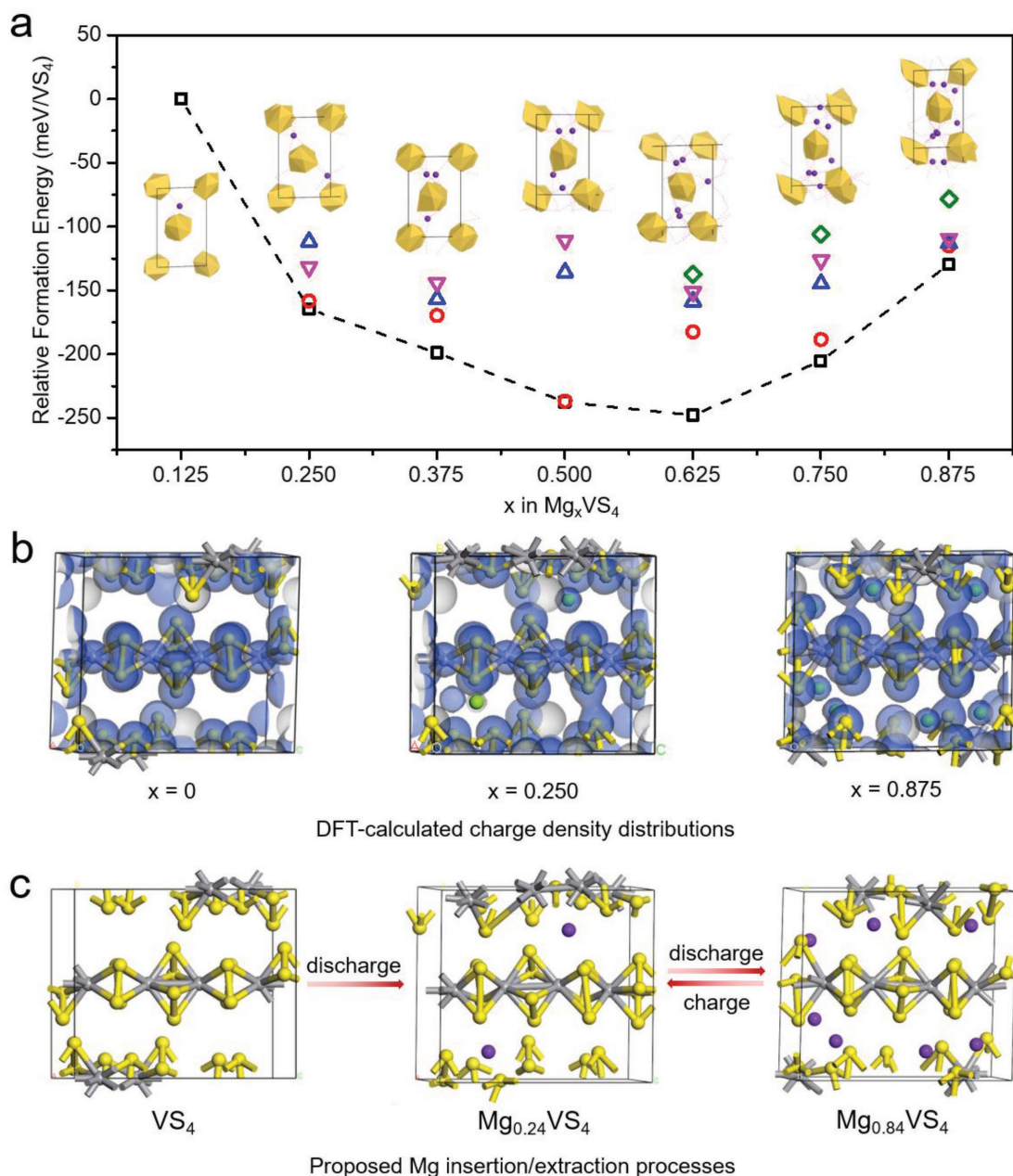$$\text{Cathode}: VS_4 + 0.24Mg^{2+} + 0.48e^- \rightarrow Mg_{0.24}VS_4 \tag{1}$$

$$Mg_{0.24}VS_4 + 0.6Mg^{2+} + 1.2e^- \leftrightarrow Mg_{0.84}VS_4 \tag{2}$$

**ADVANCED
SCIENCE NEWS**

www.advancedsciencenews.com

**ADVANCED
MATERIALS**

www.advmat.de

Figure 5. DFT calculations and schematic illustration of the reversible Mg^{2+} insertion/extraction behavior into/from VS_4. a) DFT-calculated relative formation energies for different contents of Mg^{2+} ion occupations in Mg_xVS_4 supercells. b) DFT-calculated charge density distributions (isovalue = 0.5) of Mg_xVS_4 ($x = 0$, 0.25, and 0.875, respectively). c) Schematic illustration of the reversible Mg^{2+} insertion/extraction behavior into/from VS_4 during discharge/charge processes, according to the experimental results.

$$\text{Anode}: Mg \leftrightarrow Mg^{2+} + 2e^- \tag{3}$$

This Mg^{2+} insertion/extraction mechanism is very distinct from the previous report of Li–VS_4 battery,[36] in which the eventual further reduction of $Li_{3+x}VS_4$ results in the formation of Li_2S and elemental V. In contrast, in our study, there is no formation of MgS and elemental V observed during discharge/charge processes, and the integrity and ordered structure of VS_4 atomic chains are well preserved, which ensures a superior reversibility and cycling life of Mg–VS_4 battery with high capacity retention at 500 mA g^{-1} over 800 cycles. We hope that

the exploration of nanostructural linear-chain compound VS_4 cathodes for Mg batteries may bring new inspiration to the design of high-performance electrode materials for multivalent secondary batteries.

Experimental Section

Chemicals: Triblock copolymer surfactant Pluronic F127 (Mw = 12 600, PEO106PPO70PEO106, Sigma-Aldrich), $AlCl_3$ (99.99%, Sigma-Aldrich), PhMgCl (≥99%, 2.0 M in THF solution, Aladdin), Mg

**ADVANCED
SCIENCE NEWS**

www.advancedsciencenews.com

**ADVANCED
MATERIALS**

www.advmat.de

foil (99.99%, 0.127 mm thick, Sigma-Aldrich), Carbon paper (0.19 mm thick, Toray), TAA, EG, and NH_4VO_3 were purchased from Sinopharm Chemical Reagent Co., Ltd. All reagents were used without further purification.

Synthesis of Highly Branched VS_4 Nanodendrites: Typically, 0.5 g of Pluronic F127 surfactant was dissolved in 30 mL of deionized water, and then 3 mmol of NH_4VO_3 was added into the solution. The suspension was heated to 60 °C for 20 min to form a clear pale-yellow solution. Then, 30 mL EG solution of TAA (0.5 M) was added into the above mixed solution. Subsequently, the mixed solution was stirred at 60 °C for 30 min and transferred into a 100 mL Teflon-lined stainless-steel autoclave. The autoclave was maintained at 160 °C for 12 h. The product was collected and washed with deionized water and absolute alcohol for several times and dried in a vacuum oven at 60 °C for 10 h.

For comparison, VS_4 nanospheres were also synthesized as a control sample with the same synthesis procedure but without adding surfactant F-127.

Characterizations: The samples were characterized by SEM (FEI Nova450) and TEM (JEM-2100). XRD spectra were recorded using a XRD-6000 diffractometer (Shimadzu Co., Japan), equipped with a rotating anode and a Cu Kα radiation source ($\lambda = 1.54178$ Å). Nitrogen sorption–desorption isotherms were obtained through Brunauer–Emmett–Teller (BET) analysis at 77 K on a Quantachrome Autosorb-IQ-2C instrument, and the pore-size distributions were calculated using Barret–Joyner–Halender (BJH) method. X-ray photoelectron spectra (XPS) were obtained using a PHI-5000 VersaProbe X-ray photoelectron spectrometer with an Al Kα X-ray radiation.

Electrochemical Measurements: The working cathode was prepared by adding a mixture of active material (80 wt%), conducting acetylene black (10 wt%), and polyvinylidene fluoride (PVDF, 10 wt%) into N-methyl-2-pyrrolidinone (NMP) solvent to form a homogeneous slurry, and then spread on carbon paper (as current collector) and dried in a vacuum oven at 80 °C for 12 h. The mass loading of active material is 1.5–2.0 mg cm^{-2}. Coin-type (CR2032) cells were assembled in an Ar-filled glove box with Whatman glass fiber separators and Mg foil anodes. Mg foil was polished with 600-grit SiC sandpaper and cleaned prior to use. The THF solution containing 0.4 M 2PhMgCl–AlCl$_3$ (APC) was prepared following a reported procedure and used as electrolyte.[9] The galvanostatic discharge–charge performances were measured on a LAND CT2001A multichannel battery test system between 0.2 and 2.2 V versus Mg^{2+}/Mg at room temperature. Cyclic voltammetry (CV) was performed using an electrochemistry workstation (Chenhua CHI-760E) at a scan rate of 0.2 mV s^{-1}. The GITT was performed at constant current densities (50, 100, and 150 mA g^{-1}) for 20 min followed by 2 h of open circuit period upon discharging and charging processes, respectively. The specific capacity was calculated based on the loading mass of cathode material.

Computational Details: All the calculations of Mg–VS_4 structure were performed with Dmol^3 in Material Studios software (Materials Studio version 4.0, Accelrys, Inc., San Diego, 2006). The DFT was applied to geometry optimizations at the level of PBE/DND4.4. The supercell of VS_4 was built on the basis of crystalline structure. All combinations of possible insertion positions of Mg^{2+} ions and corresponding optimized structures of Mg$_x$VS$_4$ with different Mg^{2+} insertion content x (from 0 to 0.875) with PBE functional were tested and given in Table S3 (Supporting Information), Figure 5, and Figures S11, S12, and S14 (Supporting Information). The Self-consistent field convergence criterion was set to 10^{-4}.

To reduce the influence of geometry changes on the formation energy, the relative formation energy per VS_4 unit (shown in Figure 5a) was defined as

$$\Delta E_F = E(Mg_xVS_4) - E(Mg_{x-1/n}VS_4) - \left(E(Mg_{1/n}VS_4) - E(VS_4)\right)$$

where $E(Mg_xVS_4)$ are the lowest energy state with x Mg^{2+} ions ($x = 1/n$ to 1) inserted into the VS_4, and $E(VS_4)$ is the energy of pristine VS_4. Since we carried out DFT calculations based on the supercell of V_8S_{32}, the value of n, which represents the number of VS_4 cell, is 8.

Figure S13 (Supporting Information) shows the DFT calculation results for the charge (electron) density of the inserted Mg ions (called q_{Mg}/n, as noted below). Since the formal charge of Mg^{2+} ion is taken as +2 before the insertion of Mg ion into VS_4, the value of $(2-q_{Mg}/nx)$ can reflect the average extent of electron transfer from VS_4 to each Mg ion in Mg$_x$VS$_4$ when $x = 0.125$ to 0.875 ($n = 8$).

q_{Mg}: Total charge of the inserted Mg ions in the supercell of Mg$_{8x}$V$_8$S$_{32}$

q_{Mg}/n: Total charge of the inserted Mg ions in Mg$_x$VS$_4$

$(2- q_{Mg}/nx)$: The average charge transfer per Mg ion in Mg$_x$VS$_4$.

Supporting Information

Supporting Information is available from the Wiley Online Library or from the author.

Acknowledgements

Conflict of Interest

The authors declare no conflict of interest.

Keywords

[1] D. Aurbach, Z. Lu, A. Schechter, Y. Gofer, H. Gizbar, R. Turgeman, Y. Cohen, M. Moshkovich, E. Levi, *Nature* **2000**, *407*, 724.

[2] M. Matsui, *J. Power Sources* **2011**, *196*, 7048.

[3] J. Muldoon, C. B. Bucur, T. Gregory, *Angew. Chem., Int. Ed.* **2017**, *129*, 12232.

[4] I. A. R. Pérez, Y. F. Yuan, C. Bommier, X. F. Wang, L. Ma, D. P. Leonard, M. M. Lerner, R. G. Carter, T. P. Wu, P. A. Greaney, J. Lu, X. L. Ji, *J. Am. Chem. Soc.* **2017**, *139*, 13031.

[5] M. Xu, S. l. Lei, J. Qi, Q. Y. Dou, L. Y. Liu, Y. L. Lu, Q. Huang, S. Q. Shi, X. B. Yan, *ACS Nano* **2018**, *12*, 3733.

[6] L. Wang, B. Jiang, P. E. Vullum, A. M. Svensson, A. Erbe, S. M. Selbach, H. L. Xu, F. V. Brue, *ACS Nano* **2018**, *12*, 2998.

[7] D. Aurbach, G. S. Suresh, E. Levi, A. Mitelman, O. Mizrahi, O. Chusid, M. Brunelli, *Adv. Mater.* **2007**, *19*, 4260.

[8] E. Levi, Y. Gofer, D. Aurbach, *Chem. Mater.* **2010**, *22*, 860.

[9] L. F. Wan, B. R. Perdue, C. A. Apblett, D. Prendergast, *Chem. Mater.* **2015**, *27*, 5932.

[10] N. Wu, Y. C. Lyu, R. J. Xiao, X. Q. Yu, Y. X. Yin, X. Q. Yang, H. Li, L. Gu, Y. G. Guo, *NPG Asia Mater.* **2014**, *6*, E120.

[11] H. Yoo, I. Shterenberg, Y. Gofer, G. Gershinsky, *Energy Environ. Sci.* **2013**, *6*, 2265.

[12] O. Mizrahi, N. Amir, E. Pollak, O. Chusid, V. Marks, H. Gottlieb, L. Larush, E. Zinigrad, D. Aurbach, *J. Electrochem. Soc.* **2008**, *155*, A103.

[13] R. E. Doe, R. Han, J. Hwang, A. J. Gmitter, I. Shterenberg, H. D. Yoo, N. Pour, D. Aurbach, *Chem. Commun.* **2014**, *50*, 243.

[14] O. Tutusaus, R. Mohtadi, T. S. Arthur, F. Mizuno, E. G. Nelson, Y. V. Sevryugina, *Angew. Chem., Int. Ed.* **2015**, *54*, 7900.

[15] E. N. Keyzer, H. F. J. Glass, Z. G Liu, P. M. Bayley, S. E. Dutton, C. P. Grey, D. S. Wright, *J. Am. Chem. Soc.* **2016**, *138*, 8682.

[16] S. B. Son, T. Gao, S. P. Harvey, K. X. Steirer, A. Stokes, A. Norman, C. S. Wang, A. Cresce, K. Xu, C. M. Ban, *Nat. Chem.* **2018**, *10*, 532.

[17] Y. L. Liang, R. J. Feng, S. Q. Yang, H. Ma, J. Liang, J. Chen, *Adv. Mater.* **2011**, *23*, 640.

[18] Y. W. Cheng, Y. Y. Shao, V. Raju, X. L. Ji, B. L. Mehdi, K. S. Han, M. H. Engelhard, G. S. Li, N. D. Browning, K. T. Mueller, J. Liu, *Adv. Funct. Mater.* **2016**, *26*, 3446.

[19] J. T. Incorvati, L. W. F. Wan, B. Key, D. H. Zhou, C. Liao, L. Fuoco, M. Holland, H. Wang, D. Prendergast, K. R. Poeppelmeier, J. T. Vaughey, *Chem. Mater.* **2016**, *28*, 17.

[20] L. Wang, K. Asheim, P. E. Vullum, A. M. Svensson, F. V. Bruer, *Chem. Mater.* **2016**, *28*, 6459.

[21] Q. D. Truong, M. K. Devaraju, D. N. Nguyen, Y. Gambe, K. Nayuki, Y. Sasaki, P. D. Tran, I. Honma, *Nano Lett.* **2016**, *16*, 5829.

[22] T. Koketsu, J. W. Ma, B. J. Morgan, M. Body, C. Legein, W. Dachraoui, M. Giannini, A. Demortière, M. Salanne, F. Dardoize, H. Groult, O. J. Borkiewicz, K. W. Chapman, P. Strasser, D. Dambournet, *Nat. Mater.* **2017**, *16*, 1142.

[23] D. Imamura, M. Miyayama, M. Hibino, T. Kudo, *J. Electrochem. Soc.* **2003**, *150*, A753.

[24] R. Zhang, X. Yu, K.-W. Nam, C. Ling, T. S. Arthur, W. Song, A. M. Knapp, S. N. Ehrlich, X.-Q. Yang, M. Matsui, *Electrochem. Commun.* **2012**, *23*, 110.

[25] C. Yuan, Y. Zhang, Y. Pan, X. Liu, G. Wang, D. Cao, *Electrochim. Acta* **2014**, *116*, 404.

[26] L. Wang, Z. H. Wang, P. E. Vullum, S. M. Selbach, A. M. Svensson, F. V. Bruer, *Nano Lett.* **2018**, *18*, 763.

[27] Y. L. Liang, H. D. Yoo, Y. F. Li, J. Shuai, H. A. Calderon, F. C. R. Hernandez, L. C. Grabow, Y. Yao, *Nano Lett.* **2015**, *15*, 2194.

[28] B. Liu, T. Luo, G. Mu, X. Wang, D. Chen, G. Shen, *ACS Nano* **2013**, *7*, 8051.

[29] Z. L. Tao, L. N. Xu, X. L. Gou, J. Chen, H. T. Yuan, *Chem. Commun.* **2004**, 2080.

[30] X. Q. Sun, P. Bonnick, L. F. Nazar, *ACS Energy Lett.* **2016**, *1*, 297.

[31] H. D. Yoo, Y. L. Liang, H. Dong, J. H. Lin, H. Wang, Y. S. Liu, L. Ma, T. P. Wu, Y. F. Li, Q. Ru, Y. Jing, Q. Y. An, W. Zhou, J. H. Guo, J. Lu, S. T. Pantelides, X. F. Qian, Y. Yao, *Nat. Commun.* **2017**, *8*, 339.

[32] X. Q. Sun, P. Bonnick, V. Duffort, M. Liu, Z. Q. Rong, K. A. Persson, G. Ceder, L. F. Nazar, *Energy Environ. Sci.* **2016**, *9*, 2273.

[33] H. S. Kim, T. S. Arthur, G. D. Allred, J. Zajicek, J. G. Newman, A. E. Rodnyansky, A. G. Oliver, W. C. Boggess, J. Muldoon, *Nat. Commun.* **2011**, *2*, 427.

[34] W. F. Hillebrand, *J. Am. Chem. Soc.* **1907**, *29*, 1019.

[35] R. Allmann, I. Baumann, A. Kutoglu, H. Rosch, E. Hellner, *Naturwissenschaften* **1964**, *51*, 263.

[36] S. Britto, M. Leskes, X. Hua, C.-A. Hebert, H. S. Shin, S. Clarke, O. Borkiewicz, K. W. Chapman, R. Seshadri, J. Cho, C. P. Grey, *J. Am. Chem. Soc.* **2015**, *137*, 8499.

[37] M. H. Whangbo, P. Gressier, *Inorg. Chem.* **1984**, *23*, 1228.

[38] C. S. Rout, X. Xu, J. Yang, H. Y. Jeong, D. Odkhuu, N. Park, J. Cho, H. S. Shin, *J. Am. Chem. Soc.* **2013**, *135*, 8720.

[39] T. Murugesan, S. Ramesh, J. Gopalkrishnan, C. N. R. J. Rao, *Solid State Chem.* **1982**, *44*, 119.

[40] X. Xu, S. Jeong, C. S. Rout, P. Oh, M. Ko, H. Kim, M. G. Kim, R. Cao, H. S. Shin, J. Cho, *J. Mater. Chem. A* **2014**, *2*, 10847.

[41] Y. L. Zhou, Y. L. Li, J. Yang, J. Tian, H. Y. Xu, J. Yang, W. L. Fan, *ACS Appl. Mater. Interfaces* **2016**, *8*, 18797.

[42] R. M. Sun, Q. L. Wei, Q. D. Li, W. Luo, Q. Y. An, J. Z. Sheng, D. Wang, W. Chen, L. Q. Mai, *ACS Appl. Mater. Interfaces* **2015**, *7*, 20902.

[43] G. Silvermit, D. Delpa, H. Poleman, G. B. Marin, R. D. Gryse, *J. Electron Spectrosc. Relat. Phenom.* **2004**, *135*, 167.

[44] H. J. Liu, Q. He, H. L. Jiang, Y. X. Lin, Y. K. Zhang, M. Habib, S. M. Chen, L. Song, *ACS Nano* **2017**, *11*, 11574.

[45] P. He, M. Y. Yan, G. B. Zhang, R. M. Sun, L. N. Chen, Q. Y. An, L. Q. Mai, *Adv. Energy Mater.* **2017**, *7*, 1601920.

[46] H. F. Liang, H. H. Shi, D. F. Zhang, F. W. Ming, R. R. Wang, J. Q. Zhuo, Z. C. Wang, *Chem. Mater.* **2016**, *28*, 5587.

[47] Z. Z. Karger, X. Y. Zhao, D. Wang, T. Diemant, R. J. Behm, M. Fichtner, *Adv. Energy Mater.* **2015**, *5*, 1401155.

[48] V. Augustyn, P. Simon, B. Dunn, *Energy Environ. Sci.* **2014**, *7*, 1597.

[49] D. S. Aydin, Z. Bayindir, M. O. Pekguleryuz, *J. Alloys Compd.* **2014**, *584*, 558.

[50] H. B. Yao, H. Li, A. T. S. Wee, *Electrochim. Acta* **2003**, *48*, 4197.

[51] M. N. Kozlova, Y. V. Mironov, E. D. Grayfer, A. I. Smolentsev, V. I. Zaikovskii, N. A. Nebogatikova, T. Y. Podlipskaya, V. E. Fedorov, *Chem. - Eur. J.* **2015**, *21*, 4639.

[52] M. S. Weimer, R. F. McCarthy, J. D. Emery, M. J. Bedzyk, F. G. Sen, A. Kinaci, M. K. Y. Chan, A. S. Hock, A. B. F. Martinson, *Chem. Mater.* **2017**, *29*, 2864.